GDCh

Research Article

Angewandte
Chemie
International Edition
www.angewandte.org

Electrocatalytic CO₂ Reduction

Electronic Structure Tuning in Cu–Co Dual Single Atom Catalysts for Enhanced COOH* Spillover and Electrocalytic CO₂ Reduction Activity

Yang Yang, Wenjun Zhang, Guangchen Wu, Qiang Huang, Jinghong Wen,* Dingsheng Wang,* and Mingyang Liu*

Abstract: The development of efficient electrocatalysts for CO_2 reduction to CO is challenging due to competing hydrogen evolution and intermediate over-stabilization. In this study, a Cu–Co dual single-atom catalyst (CuCo-DSAC) anchored on carbon black was synthesized via scalable pyrolysis. The catalyst achieves 98.5% CO Faradaic efficiency at 500 mA cm^{-2}, maintaining > 95% selectivity across a 400 mV window with < 6% decay over 48 h, which is superior to the corresponding single-atom control samples. In situ spectroscopy and DFT calculations reveal a synergistic mechanism: Co sites activate CO_2 and stabilize *COOH intermediates, while adjacent Cu sites facilitate CO desorption by lowering the energy barrier through charge redistribution. This dynamic buffer system mitigates active-site blocking and suppresses HER by weakening H adsorption. The electronic interplay between Cu and Co optimizes intermediate energetics, enabling industrial-level performance. This work demonstrates the potential of tailored dual-site architectures for complex electrocatalytic processes, offering a promising approach to overcoming traditional limitations.

Introduction

The escalating combustion of fossil fuels has precipitated a critical imbalance in atmospheric CO_2 levels, driving urgent demands for carbon-neutral technologies.[1,2] Electrocatalytic CO_2 reduction reaction (CO₂RR) emerges as a dual-functional solution, enabling both carbon recycling and sustainable synthesis of value-added chemicals.[3] Although laboratory-scale CO_2-to-CO conversion achieves remarkable Faradaic efficiencies (>99%) with simplified product separation,[4,5] industrial implementation remains hindered by competing hydrogen evolution reactions (HER) and insufficient energy efficiency.[6] This technological gap underscores the imperative for developing advanced electrocatalysts that reconcile atomic economy with precise reaction control.

Single-atom catalysts (SACs) represent a paradigm shift in catalytic design, offering maximized metal utilization and tunable electronic structures.[7–9] However, their isolated active sites impose geometric constraints on multistep reactions like CO₂RR, which involves sequential proton-coupled electron transfers and intermediate transformations.[10,11] Conventional SACs optimization strategies focusing solely on rate-determining step (RDS) modification face fundamental limitations in addressing complex reaction networks. Dual-single atom catalysts (DSACs) transcend these constraints through strategically paired metal centers that synergistically modulate intermediate adsorption and reaction pathways.[12–14] Copper-based systems have led CO₂-to-multicarbon conversion research due to their distinct CO/H adsorption properties.[3,15,16] However, challenges in product selectivity arise from uncontrolled C–C coupling and over-stabilization of CO intermediates.[17] The employment of rationally designed Cu–Co dual-single atom system has the potential to address these challenges by leveraging the C–C coupling capability of Cu and the enhanced CO_2 activation capacity of Co.[18] This synergy fosters the creation of a dynamic catalytic environment, characterized by enhanced activity and selectivity.

Herein, we present a rationally designed Cu–Co dual single-atom catalyst (CuCo-DSAC) on carbon black, synthesized via a scalable method. Comprehensive characterization using aberration-corrected transmission electron microscopy (AC-TEM) and X-ray absorption fine structure (XAFS) confirms the atomic dispersion and coordinated states of both metals. The CuCo-DSAC exhibits superior CO₂RR performance compared to single-metal counterparts,

[*] Y. Yang, W. Zhang, G. Wu, M. Liu
State Key Laboratory of Medicinal Chemical Biology, Tianjin Key Laboratory of Environmental Remediation and Pollution Control, College of Environmental Science and Engineering, Nankai University, Tianjin 300350, China
E-mail: mingyangliu@nankai.edu.cn

D. Wang
Department of Chemistry, Tsinghua University, Beijing 100084, China
E-mail: wangdingsheng@mail.tsinghua.edu.cn

J. Wen
School of Chemistry and Chemical Engineering, Liaocheng University, Liaocheng 252000, China
E-mail: wenjinghong@lcu.edu.cn

Q. Huang
School of Chemistry and Chemical Engineering, Nantong University, Nantong 226019, China

⌨ Additional supporting information can be found online in the Supporting Information section
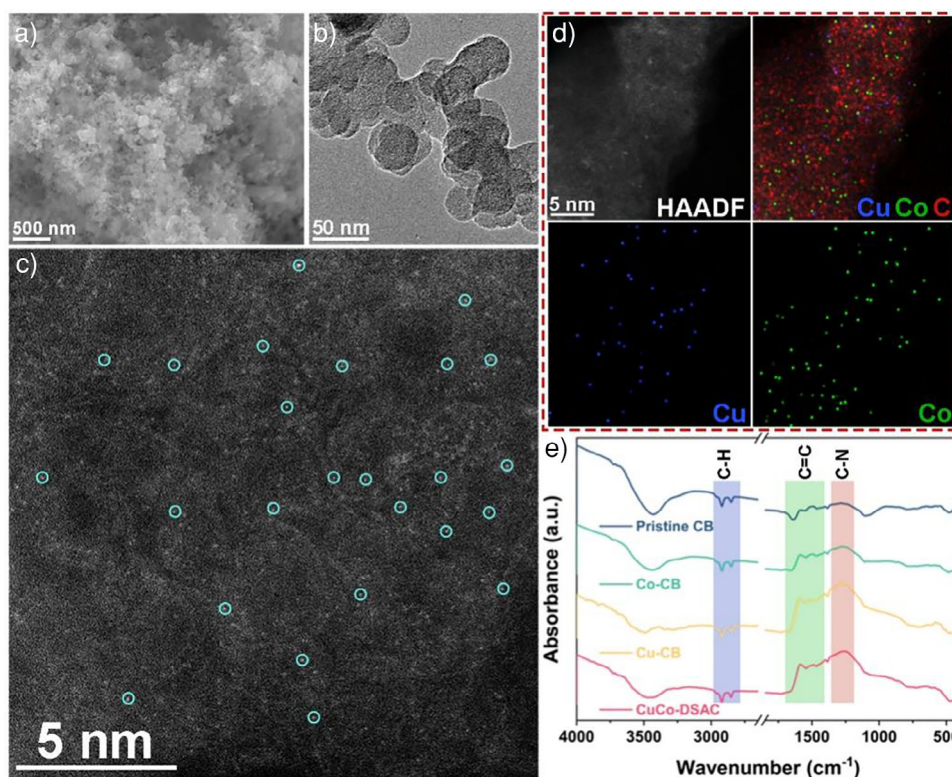
Figure 1. Physical Characterization of Catalysts. a) SEM image of CuCo-DSAC illustrating the nanoparticle morphology. b) TEM image showing the absence of visible metal particles in CuCo-DSAC. c) Atomic-resolution HAADF-TEM image revealing the uniform dispersion of Cu and Co atoms. d) Atomic-scale EDS mappings show the dispersion of Cu and Co atoms in CuCo-DSAC. e) FTIR spectra highlighting the functional groups and bond structures in the samples.

achieving a 97% Faradaic efficiency for CO in an H-cell with 0.5 M KHCO$_3$ and less than 5% decay over 10 h. In a flow cell with 1.0 M KOH, it reaches a current density of 500 mA cm^{-2} at −0.66 V with 98.5% selectivity. In situ spectroscopic and theoretical analyses reveal a cooperative mechanism: Co sites primarily drive CO$_2$ activation, while adjacent Cu atoms create an electronic buffer that stabilizes and accelerates the conversion of the critical COOH* intermediate. This synergy—where Cu mitigates intermediate accumulation by facilitating COOH* transformation and Co maintains efficient CO$_2$ adsorption—enables sustained high selectivity (>95% CO across a 400 mV range) and stability (48 h of operation with negligible degradation), establishing a new paradigm for dual-site catalytic design in multistep electrochemical conversions.

Results and Discussion

The CuCo-DSAC was synthesized via a cost-effective pyrolysis method using commercial carbon black and tailored metal precursors. Unlike single-metal analogs (Cu–CB/Co–CB), the simultaneous introduction of Cu^{2+} and Co^{2+} precursors induced mutually repulsive ionic interactions during thermal treatment (600 °C, Ar), effectively suppressing metal aggregation and promoting monomeric dispersion. This synergistic stabilization was validated by inductively coupled plasma-

mass spectrometry (ICP-MS) analysis (Table S1), showing balanced Cu/Co loading (0.49/0.24 wt%) in CuCo-DSAC, compared to asymmetric retention in single-metal systems (Cu–CB: 0.22 wt% Cu; Co-CB: 0.32 wt% Co).

This disparity arises from the metals' divergent coordination dynamics. In single-metal systems, Cu's strong π-backbonding with pyridinic-N promotes aggregation, while Co's preferential tetrahedral coordination with pyrrolic N enhances dispersion. Bimetallic synergy alters these tendencies—Cu–Co charge transfer disrupts Cu's aggregation propensity, while Co's coordination stabilizes Cu atoms. To ensure fair performance comparisons, control samples with matched metal contents were prepared through precursor dosage adjustments, ensuring equivalent active site densities across all catalysts. This methodology establishes a generalizable approach for stabilizing incompatible metal pairs in atomically dispersed configurations.

The atomic dispersion of metal species was systematically verified through multi-technique characterization. X-ray diffraction (XRD) patterns of all catalysts showed broad graphene carbon peaks at 24° and 44°, with no metallic phase signatures, indicating atomic-scale metal distribution (Figure S1). Morphological analysis via scanning electron microscope (SEM)/TEM confirmed the preservation of carbon black's nanoparticle architecture post-pyrolysis, with no observable metal clusters (Figure 1a,b, Figures S2 and S3). Elemental mapping demonstrated a homogeneous spatial distribution of
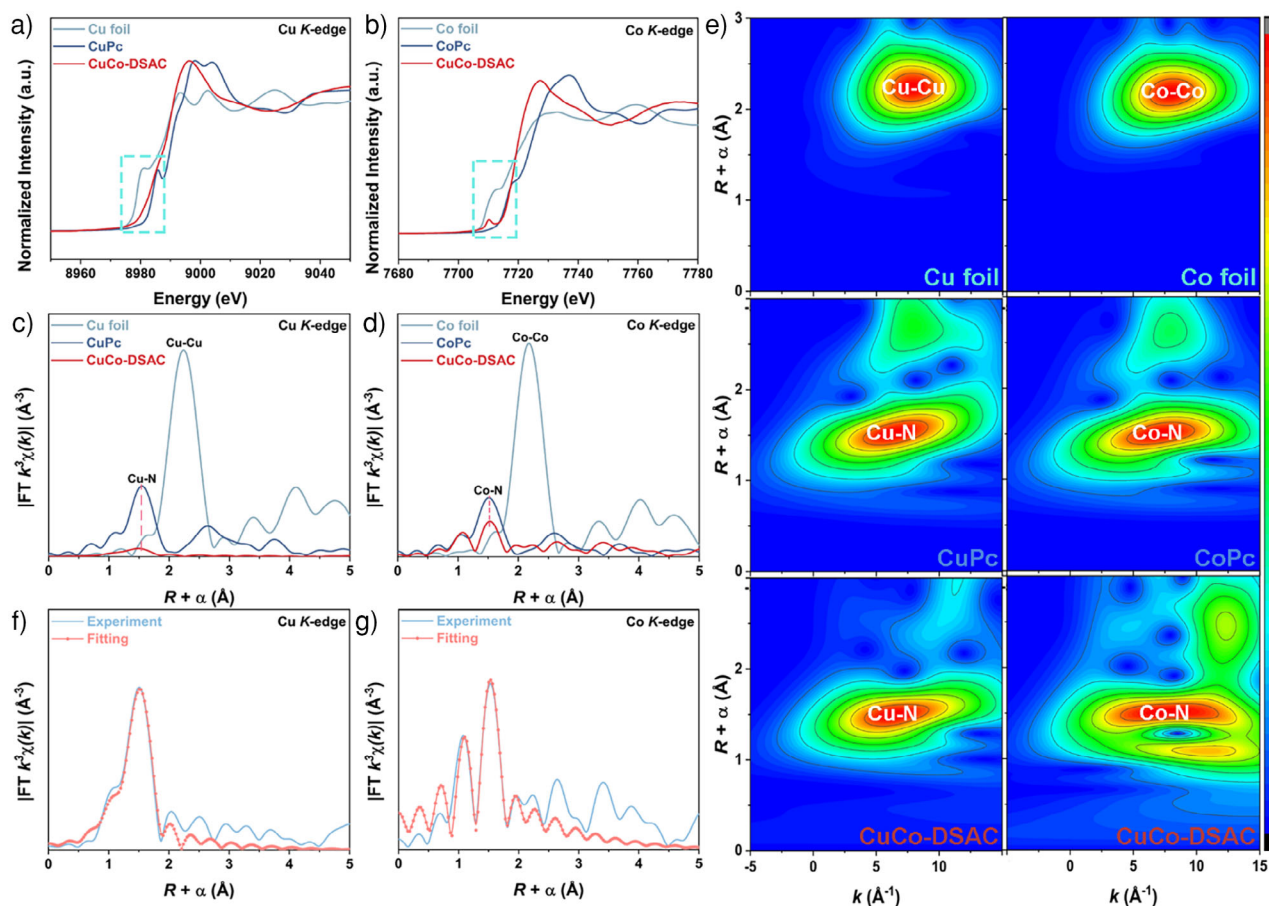
Figure 2. Coordination structure analysis of CuCo-DSAC. a) Normalized Cu K-edge XANES spectrum showing copper's electronic state. b) Normalized Co *K*-edge XANES spectrum indicating cobalt's electronic state. c) Cu *K*-edge FT-EXAFS spectrum in *R*-space, illustrating coordination environment. d) Co *K*-edge FT-EXAFS spectrum in *R*-space, detailing coordination structure. e) Wavelet transforms of k^3-weighted EXAFS signals, differentiating backscattering atoms. f) Cu *K*-edge EXAFS data (points) and curve fit (line) for CuCo-DSAC, shown in *R*-space. g) Co *K*-edge EXAFS data (points) and curve fit (line) for CuCo-DSAC, shown in *R*-space.

Cu/Co–N–C motifs (Figures S4-S6), while high angle annular dark field (HAADF)-STEM explicitly revealed isolated metal atoms in CuCo-DSAC (Figure 1c), contrasting with aggregated species in Cu–CB and Co–CB (Figure S7). Atomic-level energy dispersive spectrometer (EDS) mappings have been shown to provide precise indications of the dispersion of Cu and Co atoms in CuCo-DSAC (Figure 1d). This confirms that Cu–Co ionic repulsion during synthesis effectively prevents metal agglomeration.

Spectroscopic investigations further elucidated chemical bonding evolution. Fourier transform infrared spectroscopy (FTIR) spectra showed intensified C≡C/C─N vibrations at 1588 and 1270 cm^{-1},[19–21] proportional to metal loading, indicating enhanced metal-N─C coordination (Figure 1e). X-ray photoelectron spectroscopy (XPS) analysis revealed critical bonding transformations (Figures S8): the emergence of pyridinic-N at 398.6 eV in metal-containing samples compared to pristine carbon (Figure S8d),[22,23] and selective preservation of C─O groups over C═O species post-pyrolysis (Figures S8b,c).[24–26] Although surface metal concentrations remained below XPS detection limits, XAFS analysis complemented these findings by resolving metal coordination

states. These results establish that dual-metal incorporation modifies the carbon electronic structure through selective N coordination while maintaining atomic dispersion via synergistic ionic interactions.

XAFS spectroscopy elucidated the electronic and coordination structures of Cu/Co centers in CuCo-DSAC. X-ray absorption near-edge structure (XANES) analysis positioned the Cu *K*-edge between metallic Cu and CuPc (Figure 2a), indicating a mixed valence state ($0 < \delta < +2$), while the Co *K*-edge aligned with CoPc (Figure 2b), confirming a + 2 oxidation state. Fourier-transformed extended X-ray absorption fine structure (EXAFS) spectra revealed dominant Cu–N and Co–N coordination shells at 1.5 Å, with no metal-metal scattering paths (2.2 Å) present, as seen in foil references (Figures 2c,d). Wavelet transform analysis further resolved nitrogen-coordination signatures, with CuCo-DSAC showing intensity maxima at coordinates matching CuPc/CoPc references (Figure 2e), confirming atomic dispersion. Quantitative EXAFS fitting established distinct coordination geometries (Figure 2f,g, Figures S9–S10): Cu centers adopted square-planar Cu–N$_4$ configurations, while Co formed octahedral Co–N$_6$ sites (Tables S2-S3). The absence of Cu–Co/Cu–Cu/
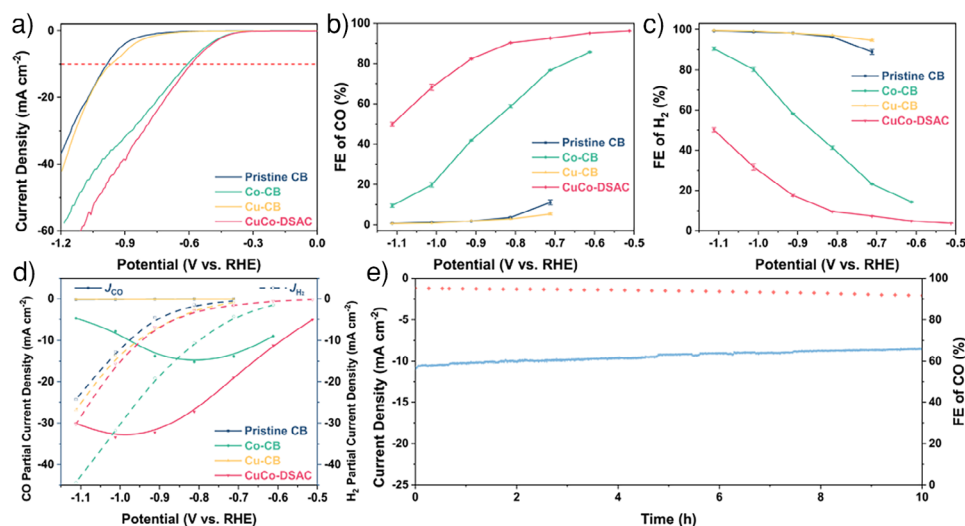
Figure 3. Catalytic performance of CO_2 electroreduction to CO. a) LSV curves comparing the electrochemical activity of different catalysts (0.5 M $KHCO_3$, 20 sccm CO_2 flow). b) Potential-dependent Faradaic efficiencies for CO production across samples. c) Potential-dependent Faradaic efficiencies for H_2 production across samples. d) Potential-dependent partial current densities for CO and H_2. e) Stability evaluation of CuCo-DSAC via chronoamperometric test at -0.6 V versus RHE over 10 h.

Co–Co scattering paths and low Debye–Waller factors corroborates the dual-isolated atomic architecture.

CuCo-DSAC demonstrated superior CO_2RR activity in an H-cell with 0.5 M $KHCO_3$, showing a low onset potential of -0.4 V versus RHE, outperforming controls (pristine CB: -0.76 V; Cu–CB: -0.72 V; Co–CB: -0.41 V) (Figure 3a). At -1.0 V, it achieved 48 mA cm^{-2} with a 97% CO Faradaic efficiency (FE) at -0.51 V, sustained above 90% across a 300 mV window (Figure 3b–d). Triplicate measurements showed minimal variability, achieved through standardized electrode fabrication and precise gas chromatography calibration. Systematic screening of Cu/Co ratios revealed that Co content primarily governs FE, while Cu modulates current density (Table S4), with CuCo-DSAC delivering an optimal balance. Enhanced activity correlates with its high electrochemical surface area ($C_{dl} = 10.45$ mF cm^{-2}) and intermediate charge transfer resistance (Figures S11 and S12), reflecting synergistic interface engineering. Stability tests confirmed less than 5% FE decay over 10 h at -0.6 V (Figure 3e).

In a gas diffusion flow cell with 1.0 M KOH, CuCo-DSAC achieved 500 mA cm^{-2} at -0.66 V with 98.5% CO selectivity, maintaining over 95% across -0.1 to -0.5 V (Figure 4a–c). The CO turnover frequency (1522 h^{-1} at -0.6 V) surpassed Co–CB by 3.5-fold (Figure 4d), with batch-to-batch FE variations constrained to less than 5% through flow rate stabilization and consistent electrolyte batches. Preliminary findings from durability tests indicate a loss of selectivity of less than 6% after 48 h, with a current density loss rate of 0.85 mA h^{-1} (Figure 4e). Post-reaction characterization confirmed the structural integrity of CuCo-DSAC after prolonged operation. SEM analysis showed preserved catalyst morphology with no particle aggregation (Figure S13a), while AC-TEM/EDS mapping verified sustained atomic dispersion of Cu and Co species, with only minor localized clustering (Figure S13b,c). XPS spectra indicated consistent chemical

states for Co, Cu, and N before and after testing, with detected fluorine attributed to residual binder components from electrode fabrication (Figure S13d).

The synthesis protocol demonstrated exceptional scalability, producing 10.3 g per batch without compromising performance (Figure S14a). Bulk-synthesized catalysts achieved identical CO partial current densities compared to lab-scale counterparts (Figure S14b), with AC-TEM confirming the preserved atomic dispersion of both metals (Figure S14c). This reproducibility across production scales, combined with low material costs, positions CuCo-DSAC as a viable candidate for industrial implementation.

Comparisons with advanced alternative catalysts identify CuCo-DSAC as a cost-effective, high-performance alternative to precious metal and nanoparticle systems in industrial CO_2 electrolysis, excelling in efficiency, stability, cost, and scalability (Table S5). Key variability sources—electrode homogeneity, GC calibration drift, and electrolyte impurities—were systematically mitigated. Performance metrics across three independently synthesized batches showed less than 8% deviation in current density and less than 5% in FE, validating protocol robustness. This rigorous error control establishes CuCo-DSAC as a high-fidelity catalyst for scalable CO_2-to-CO conversion.

In situ surface-enhanced Raman spectroscopy (SERS) and attenuated total reflection surface-enhanced infrared absorption spectroscopy (ATR-SEIRAS) analyses provide critical insights into the dynamic roles of Cu and Co single-atom sites in CuCo-DSAC during CO_2 electroreduction (Figure 5a,b). At open-circuit potential (OCP), all catalysts (CuCo-DSAC, Cu–CB, Co–CB) exhibit characteristic D ($\sim$1332 cm^{-1}) and G ($\sim$1580 cm^{-1}) bands of graphitic carbon,[27] along with peaks corresponding to adsorbed bicarbonate (HCO$_3^-$, 1013 cm^{-1}) and carbonate (CO$_3^{2-}$, 1071 cm^{-1}).[28] Notably, the weaker intensity of the *COOH-related band ($\sim$1580 cm^{-1}) in
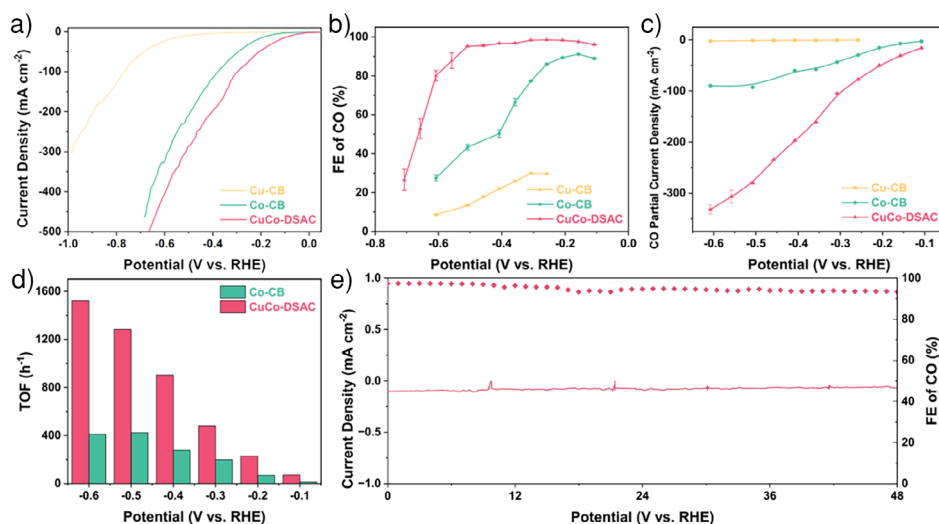
Figure 4. CO_2RR performance in a flow cell. a) LSV curves, b) potential-dependent Faradic efficiencies of CO for Cu–CB, Co–CB, and CuCo-DSAC in 1.0 M KHCO₃ electrolyte (three independent tests calculated the error bars). c) Potential-dependent CO partial current densities for different samples. d) Turnover frequency of Co–CB, and CuCo-DSAC. e) The current density change and CO Faradaic efficiency change of CuCo-DSAC under −0.3 V versus RHE for 48 h in a flow cell system.
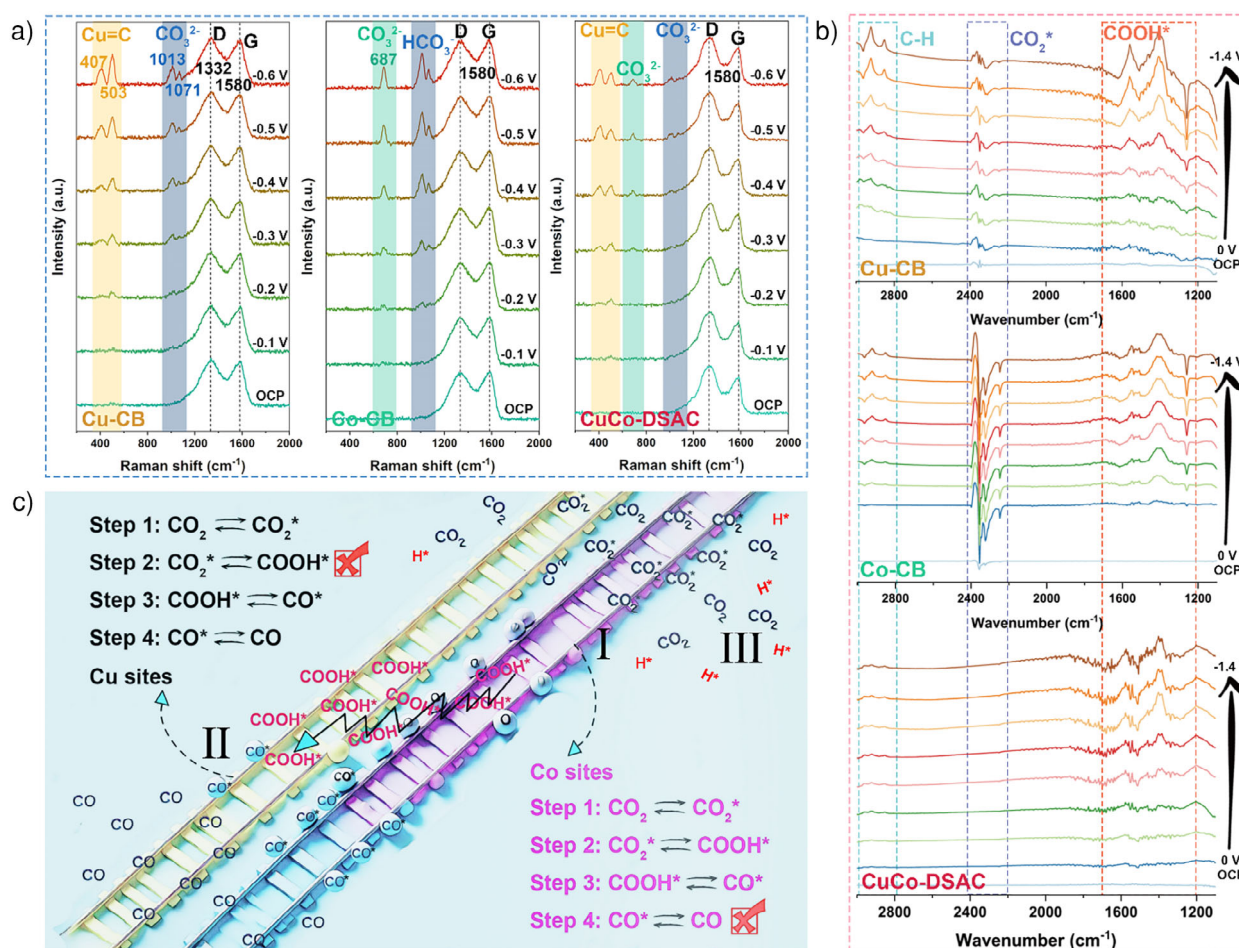
Figure 5. In situ ATR- SEIRAS and SERS characterization. a) In situ SERS spectra of Cu–CB, Co–CB, and CuCo-DSAC as a function of potential. b) In situ ATR-SEIRAS spectra recorded on Cu–CB, Co–CB, and CuCo-DSAC in CO_2-saturated 0.5 M KHCO₃ solution. The spectra were collected at constant potentials with 0.2 V interval. c) The following schematic illustrates the CO_2 reduction pathways for the copper (yellow rails) and cobalt sites (purple rails).
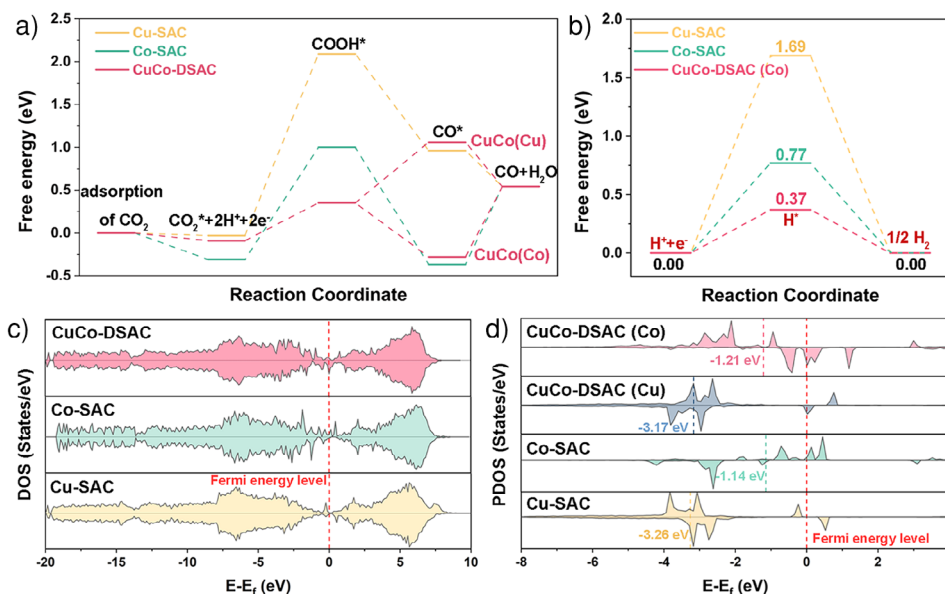
Figure 6. Mechanism investigation during the CO_2RR process. Free energy profiles at $U = 0$ V of a) CO_2RR, and b) HER. c) The density of states (DOS) and d) partial DOS (PDOS) for the Cu-SAC, Co-SAC, and CuCo-DSAC.

CuCo-DSAC compared to Co–CB indicates accelerated *COOH intermediate conversion,[29] underscoring the synergistic mitigation of intermediate accumulation.

Under applied potentials, distinct spectral features emerge that differentiate the catalytic behaviors of Cu–CB, Co–CB, and CuCo-DSAC. Cu–CB develops peaks at 407 and 503 cm^{-1}, assigned to Cu–C/Cu–CO species,[30,31] indicative of CO adsorption on Cu sites. Co–CB exhibits a gradually intensifying peak at 687 cm^{-1}, attributed to CO_3^{2-} accumulation due to excessive CO_2 adsorption. In contrast, CuCo-DSAC uniquely displays both Cu–C (503 cm^{-1}) and CO_3^{2-} (687 cm^{-1}) signals, albeit with reduced intensities compared to single-metal catalysts. This suggests enhanced reaction kinetics, where Cu sites facilitate *COOH spillover and CO desorption, while Co sites maintain efficient CO_2 activation, minimizing CO_3^{2-} formation.

ATR-SEIRAS further resolves the reaction pathways by analyzing oscillatory bands associated with *COOH intermediates (1200–1660 cm^{-1}) at low potentials (−0.3 V vs. RHE).[32–34] Co–CB and CuCo-DSAC both show enhanced *COOH signals, confirming Co's role in CO_2 activation and *COOH stabilization. However, Co–CB suffers from *COOH overaccumulation at higher potentials, leading to site blockage and activity decay. In contrast, CuCo-DSAC leverages neighboring Cu sites to accept *COOH intermediates via spillover, as evidenced by simultaneous signals of *COOH (1580 cm^{-1}) and CO_3^{2-} (687 cm^{-1}) reduction. This two-site synergy ensures rapid conversion of *COOH to CO, maintaining high activity across a wide potential window. The suppressed CO_3^{2-} and *COOH intensities in CuCo-DSAC, compared to Co–CB and Cu–CB, directly correlate with its superior CO selectivity (>95% Faradaic efficiency) and long-term stability. This mechanistic framework, derived from in situ spectroscopic data, establishes the complementary roles of Cu and Co sites (Figure 5c): Co activates CO_2 and stabi-

lizes *COOH intermediates, while Cu prevents intermediate accumulation by promoting spillover and CO desorption. The absence of such synergistic interactions in SACs underscores the critical importance of dual-site engineering in optimizing CO_2RR performance.

Density functional theory (DFT) calculations validate the experimental observations and elucidate the origin of CuCo-DSAC's exceptional activity. Theoretical calculations constructed structural models (Figure S15), and charge density differences for Cu–CB, Co–CB, and CuCo-DSAC were computed (Figure S16). Free energy profiles reveal distinct reaction pathways at Cu and Co sites (Figure 6a,b, Figure S17). Co sites in CuCo-DSAC exhibit a lower energy barrier for CO_2 activation (ΔG_{*COOH} = 0.35 eV) compared to Cu-SAC (2.12 eV), consistent with accelerated *COOH formation observed in ATR-SEIRAS. However, Co's strong CO adsorption (ΔG_{*CO} = 0.82 eV) prevented rapid desorption of CO. Conversely, Cu sites in CuCo-DSAC exhibit weaker *CO binding (ΔG_{*CO} = −0.52 eV), enabling efficient CO desorption and shifting the RDS to *COOH generation. This complementary behavior results in CuCo-DSAC theoretically outperforming both Cu-SAC and Co-SAC in limiting potentials and activity, in agreement with experimental results (Figure S18).

The enhanced selectivity of CuCo-DSAC is further rationalized by its thermodynamic advantage ($U_L(CO_2)$–$U_L(H_2)$), which reflects a wider gap between CO_2RR and HER (Figures S19). This arises from electronic structure modulation (Figures 6c,d): the d-band centers of Co (−1.21 eV) and Cu (−3.17 eV) in CuCo-DSAC balance intermediate adsorption strength. Co's moderate d-band center stabilizes *COOH intermediates, while Cu's electron-deficient state weakens *CO binding and raises the *H adsorption energy of Co site (ΔG_{*H} = 0.37 eV vs. Co-SAC), suppressing HER. Partial density of states (PDOS) and the charge density

difference analysis confirm charge redistribution between Cu and Co, optimizing their respective roles in CO_2 activation and intermediate management.

The synergy between Cu and Co sites is mechanistically unified as follows: 1) Co sites drive CO_2 adsorption and *COOH formation at low potentials, as evidenced by ATR-SEIRAS; 2) Cu sites accept *COOH overflow from Co via spillover, accelerating CO desorption and preventing site blocking, as indicated by reduced *COOH and CO_3^{2-} intensities in SERS; 3) electronic interplay expands the CO-selective potential window ($\Delta U = 400\,mV$), sustaining $> 95\%$ Faradaic efficiency at high current densities. This dual-site synergy overcomes the limitations of SACs, creating a dynamic buffer system that decouples CO_2 adsorption from CO desorption.

Although Cu sites lack intrinsic CO_2 activation capability, their proximity to Co creates a dynamic buffer system that reconciles conflicting steps in multistep electrocatalysis. This work highlights the potential of dual-site engineering to optimize CO_2RR performance by tailoring electronic and spatial interactions. The findings provide a roadmap for designing adaptive catalysts that achieve high activity, selectivity, and stability through targeted electronic modulation, offering scalable solutions for industrial CO_2 electroreduction applications.

This buffer architecture achieves two key advancements over traditional mechanisms. First, dynamic intermediate management ensures continuous *COOH spillover from Co to Cu, preventing active-site blocking and sustaining $> 95\%$ CO selectivity across a 400 mV window. Second, electronic resilience is enhanced as the Cu buffer stabilizes Co sites against over-reduction, maintaining 90% of initial activity after 48 h. Although Cu sites lack intrinsic CO_2 activation capability, their role as electronic modulators enables cost-effective synthesis using scalable pyrolysis. Further optimization could involve tailoring Cu coordination environments to enhance charge transfer efficiency or introducing ternary elements to refine intermediate binding gradients. This work establishes a paradigm for designing adaptive catalytic systems that reconcile high activity with operational stability in multistep electrocatalysis.

Conclusion

In conclusion, this study successfully synthesized low-cost CoCu-DSACs using a straightforward pyrolysis method. These catalysts can be produced in large quantities and effectively catalyze the reduction of CO_2 to CO. The FE for CO is high, exceeding 97%, and remains above 90% over a 300 mV potential window in an H-type cell. In a gas flow cell, the FE for CO reaches 98.5% and stays above 95% across a 400 mV potential window. Additionally, the catalyst demonstrates excellent durability in long-term tests at high current densities. The introduction of Cu single atoms alter the electronic structure of the Co sites and also functions as sites for COOH* spillover, thereby forming a buffer system, as evidenced by both in situ tests and theoretical calculations. This modification enhances the activity and selectivity of the CuCo-DSAC catalyst while expanding its active potential window. This approach, which involves the addition of step-specific active sites, offers novel insights into the development of catalysts for intricate reaction systems.

Experimental Section

Please see the Supporting Information for the detailed process.

Conflict of Interests

The authors declare no conflict of interest.

Data Availability Statement

The data that support the findings of this study are available in the supplementary material of this article.

[1] J. E. Huang, F. Li, A. Ozden, A. Sedighian Rasouli, F. P. García de Arquer, S. Liu, S. Zhang, M. Luo, X. Wang, Y. Lum, Y. Xu, K. Bertens, R. K. Miao, C.-T. Dinh, D. Sinton, E. H. Sargent, *Science* **2021**, *372*, 1074–1078.

[2] L. Guo, J. Zhou, F. Liu, X. Meng, Y. Ma, F. Hao, Y. Xiong, Z. Fan, *ACS Nano* **2024**, *18*, 9823–9851.

[3] D. Ma, C. Zhi, Y. Zhang, J. Chen, Y. Zhang, J.-W. Shi, *ACS Nano* **2024**, *18*, 21714–21746.

[4] L. Lin, H. Li, Y. Wang, H. Li, P. Wei, B. Nan, R. Si, G. Wang, X. Bao, *Angew. Chem. Int. Ed.* **2021**, *60*, 26582–26586.

[5] J.-D. Yi, D.-H. Si, R. Xie, Q. Yin, M.-D. Zhang, Q. Wu, G.-L. Chai, Y.-B. Huang, R. Cao, *Angew. Chem. Int. Ed.* **2021**, *60*, 17108–17114.

[6] J. Feng, H. Gao, L. Zheng, Z. Chen, S. Zeng, C. Jiang, H. Dong, L. Liu, S. Zhang, X. Zhang, *Nat. Commun.* **2020**, *11*, 4341.

[7] T. Gan, D. Wang, *Nano Res.* **2024**, *17*, 18–38.

[8] L. Wang, J. Wu, S. Wang, H. Liu, Y. Wang, D. Wang, *Nano Res.* **2024**, *17*, 3261–3301.

[9] C. Ren, Y. Cui, Q. Li, C. Ling, J. Wang, *J. Am. Chem. Soc.* **2025**, https://doi.org/10.1021/jacs.5c00643.

[10] W. Zhang, Y. Chao, W. Zhang, J. Zhou, F. Lv, K. Wang, F. Lin, H. Luo, J. Li, M. Tong, E. Wang, S. Guo, *Adv. Mater.* **2021**, *33*, 2102576.

[11] J. Zhang, Q.-a. Huang, J. Wang, J. Wang, J. Zhang, Y. Zhao, *Chin. J. Catal.* **2020**, *41*, 783–798.

[12] Y. Wang, F. Ma, G. Zhang, J. Zhang, H. Zhao, Y. Dong, D. Wang, *Nano Res.* **2024**, *17*, 9397–9427.

[13] F. Ma, P. Zhang, X. Zheng, L. Chen, Y. Li, Z. Zhuang, Y. Fan, P. Jiang, H. Zhao, J. Zhang, Y. Dong, Y. Zhu, D. Wang, Y. Wang, *Angew. Chem. Int. Ed.* **2024**, *63*, e202412785.

[14] S. Chen, X. Zheng, P. Zhu, Y. Li, Z. Zhuang, H. Wu, J. Zhu, C. Xiao, M. Chen, P. Wang, D. Wang, Y.-L. He, *Angew. Chem. Int. Ed.* **2024**, *63*, e202411591.

[15] X. Wang, K. Klingan, M. Klingenhof, T. Möller, J. Ferreira de Araújo, I. Martens, A. Bagger, S. Jiang, J. Rossmeisl, H. Dau, P. Strasser, *Nat. Commun.* **2021**, *12*, 794.

[16] S. Guria, D. Dolui, C. Das, S. Ghorai, V. Vishal, D. Maiti, G. K. Lahiri, A. Dutta, *Nat. Commun.* **2023**, *14*, 6859.

[17] A. Bagger, W. Ju, A. S. Varela, P. Strasser, J. Rossmeisl, *Catal. Today* **2017**, *288*, 74–78.

[18] H. Zhang, Y. Wang, S. Zuo, W. Zhou, J. Zhang, X. W. D. Lou, *J. Am. Chem. Soc.* **2021**, *143*, 2173–2177.

[19] Y.-L. Fan, X.-W. Cheng, J.-B. Wu, M. Liu, F.-Z. Zhang, Z. Xu, L.-S. Feng, *Eur. J. Med. Chem.* **2018**, *146*, 1–14.

[20] E. Håkansson, T. Lin, H. Wang, A. Kaynak, *Synth. Met.* **2006**, *156*, 1194–1202.

[21] M. Chattanahalli Devendrachari, G. Shimoga, S.-H. Lee, Y.-H. Heo, H. Makri Nimbegondi Kotresh, R. R. Palem, S.-Y. Kim, D.-S. Choi, *ACS Appl. Energy Mater.* **2023**, *6*, 11199–11211.

[22] X. Liu, L. Li, W. Zhou, Y. Zhou, W. Niu, S. Chen, *ChemElectroChem* **2015**, *2*, 803–810.

[23] W. Niu, L. Li, X. Liu, N. Wang, J. Liu, W. Zhou, Z. Tang, S. Chen, *J. Am. Chem. Soc.* **2015**, *137*, 5555–5562.

[24] Z. Ahmad, M. A. Najeeb, R. A. Shakoor, A. Alashraf, S. A. Al-Muhtaseb, A. Soliman, M. K. Nazeeruddin, *Sci. Rep.* **2017**, *7*, 15406.

[25] A. Abbasi, T. T. S. de Oliveira, G. D. Bothun, A. Bose, *ACS Appl. Nano Mater* **2020**, *3*, 2605–2613.

[26] Y. He, P. Bai, S. Gao, Y. Xu, *ACS Appl. Mater. Interfaces* **2018**, *10*, 41380–41388.

[27] S. Rodrigues, M. Marques, I. Suárez-Ruiz, I. Camean, D. Flores, B. Kwiecinska, *Int. J. Coal Geol.* **2013**, *111*, 67–79.

[28] I. V. Chernyshova, P. Somasundaran, S. Ponnurangam, *Proc. Natl. Acad. Sci* **2018**, *115*, E9261–E9270.

[29] Q. Qi, W. Shen, M. Cai, J. Cai, B. Hu, D. Han, X. Tang, Z. Zhu, P. Huo, *ACS Appl. Nano Mater* **2024**, *7*, 24788–24797.

[30] M. Moradzaman, G. Mul, *ChemElectroChem* **2021**, *8*, 1478–1485.

[31] I. Oda, H. Ogasawara, M. Ito, *Langmuir* **1996**, *12*, 1094–1097.

[32] K. Huang, R. Li, H. Qi, S. Yang, S. An, C. Lian, Q. Xu, H. Liu, J. Hu, *ACS Catal.* **2024**, *14*, 8889–8898.

[33] S. J. Lee, S. W. Han, M. Yoon, K. Kim, *Vib. Spectrosc.* **2000**, *24*, 265–275.

[34] E. Garand, T. Wende, D. J. Goebbert, R. Bergmann, G. Meijer, D. M. Neumark, K. R. Asmis, *J. Am. Chem. Soc.* **2010**, *132*, 849–856.